Check for updates

ADVANCED ENERGY MATERIALS
www.advenergymat.de

Influence of Post-Synthesis Processing on the Structure, Transport, and Performance of the Solid Electrolyte $Li_{5.5}PS_{4.5}Cl_{1.5}$ in All-Solid-State Batteries

*Oliver Maus, Martin A. Lange, Finn Frankenberg, Florian Stainer, Vasiliki Faka, Eva Schlautmann, Carolin Rosenbach, Anna Jodlbauer, Johannes Schubert, Jürgen Janek, Cheng Li, Peter Michalowski, H. Martin R. Wilkening, Arno Kwade, and Wolfgang G. Zeier**

While post-synthesis processing steps are frequently applied in the preparation of cathode composites for solid-state batteries to ensure homogeneous mixing and good contact with the cathode active material, little is known about the processes that occur during milling and how they influence structure and transport of solid electrolytes. Here, an extensive set of experimental methods and simulations are used to study the effects of post-synthesis milling by a frequency and planetary ball mill on the highly conducting chloride-rich argyrodite $Li_{5.5}PS_{4.5}Cl_{1.5}$. Structural analyses show that processing can reduce the coherence length and increase the disorder. The reduced crystallite size correlates with a decrease in ionic conductivity in the post-processed solid electrolytes. Simulating the ball milling processes by the discrete element method provides fundamental understanding and reveals the correlation of the loss in coherence with the specific energy input and the numbers of stressing events during the milling process. An observed decrease in particle size in ball milled samples leads to lower tortuosity in the cathode composites. As the loss in coherence and decrease in particle size have opposite effects on the performance, optimizing these processing conditions will play a significant role on the road to highly performing solid-state batteries.

1. Introduction

The ongoing decarbonization and electrification of the mobility sector and other industrial sectors increases the demand in highly performing energy storage systems. All-solid-state batteries have the potential to achieve higher energy densities than conventional liquid lithium ion batteries[1] by enabling the use of lithium metal[2,3] or silicon alloys[4,5] as negative electrode. To achieve sufficient power densities, solid-state batteries require optimized solid electrolytes with an ionic conductivity above 10 mS cm^{-1}.[6] Over the last years, promising Li^+ ionic conductors in the classes of oxides, e.g. $Li_7La_3Zr_2O_{12}$,[7–9] halides, e.g Li_3MCl_6 (metal cation M^{3+} = e.g., Y, Er, In),[10,11] and thiophosphates, e.g. $Li_{10}GeP_2S_{12}$,[12,13] have been studied. The thiophosphate-based lithium argyrodite with a chemical

O. Maus, M. A. Lange, V. Faka, E. Schlautmann, C. Rosenbach, W. G. Zeier
Institute of Inorganic and Analytical Chemistry
University of Münster
Corrensstraße 28-30, D-48149 Münster, Germany
E-mail: wzeier@uni-muenster.de

O. Maus, W. G. Zeier
International Graduate School for Battery Chemistry, Characterization, Analysis, Recycling and Application (BACCARA)
University of Münster
Corrensstraße 40, D-48149 Münster, Germany

The ORCID identification number(s) for the author(s) of this article can be found under https://doi.org/10.1002/aenm.202403291

© 2024 The Author(s). Advanced Energy Materials published by Wiley-VCH GmbH. This is an open access article under the terms of the Creative Commons Attribution License, which permits use, distribution and reproduction in any medium, provided the original work is properly cited.

DOI: 10.1002/aenm.202403291

F. Frankenberg, P. Michalowski, A. Kwade
Institute for Particle Technology
Technische Universität Braunschweig
Volkmaroder Straße 5, D-38104 Braunschweig, Germany

F. Stainer, A. Jodlbauer, H. M. R. Wilkening
Institute of Chemistry and Technology of Materials
Graz University of Technology (NAWI Graz)
Stremayrgasse 9, Graz A-8010, Austria

J. Schubert, J. Janek
Institute of Physical Chemistry
Justus Liebig University
Heinrich-Buff-Ring 17, D-35392 Giessen, Germany

J. Schubert, J. Janek
Center for Materials Research (ZfM)
Justus Liebig University
Heinrich-Buff-Ring 16, D-35392 Giessen, Germany

C. Li
Neutron Science Division
Oak Ridge National Laboratory
Oak Ridge, TN 37830, USA

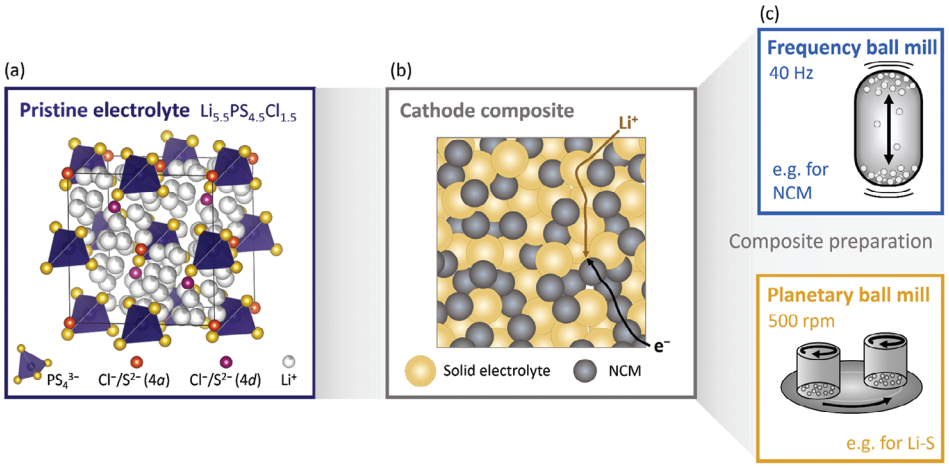


Figure 1. a) Crystal structure of the pristine $Li_{5.5}PS_{4.5}Cl_{1.5}$. b) Cathode composite of solid electrolyte and cathode active material needs to ensure sufficient ionic and electronic transport. c) Schematic representation of the working principles of the frequency ball mill and the planetary ball mill that are amongst the main methods of processing for solid-state battery building.

formula of Li_6PS_5X (halide anion X = Cl, Br, I) has gained particular interest for applications due to its high ionic conductivity and relatively simple preparation.[14]

The argyrodite structure type (**Figure 1a**) exhibits *F*43m space group symmetry in which the halide ions are located on a face-centered cubic sublattice (Wyckoff 4*a* position).[15] The PS_4^{3-} polyanions are filling the octahedral voids (P on Wyckoff 4*b*, S on 16*e*) while half of the tetrahedral voids are occupied by S^{2-} ions (Wyckoff 4*d*). Lithium ions (Wyckoff 48 h) are forming partially occupied cages around the 4*d* position that allows rapid Li^+ diffusion.[16] In Li_6PS_5Cl, a site disorder between S^{2-} and Cl^- on the 4*d* and 4*a* is observed due to the similar ionic radii.[17,18] It is reported that the lower charge of Cl^- on the 4*d* position facilitates the interconnection of the Li^+ cages and thereby increase the Li^+ ionic conductivity.[19] The effect can be enhanced by substituting S^{2-} by Cl^- in $Li_{5.5}PS_{4.5}Cl_{1.5}$ to achieve an ionic conductivity of 7 – 8 mS cm^{-1}.[20] This high conductivity makes $Li_{5.5}PS_{4.5}Cl_{1.5}$ one of the most promising materials for high performing solid-state batteries.

A sufficiently high ionic conductivity is in particular needed in electrode composites (Figure 1b) where a good conduction and contact with the active material is crucial to access full capacities.[21] To reproducibly prepare homogeneous composites and ensure best connectivity, a mixing step is usually applied. Common processing methods include the use of a frequency ball mill (see schematic in Figure 1c) as applied in various publications with $LiNi_xCo_yMn_{1-x-y}O_2$ (NCM)[22,23] as cathode active material, while planetary ball mills are frequently used for lithium-sulfur solid-state batteries[24,25] as well as NCM-sulfide composites.[26]

W. G. Zeier
Institute of Energy Materials and Devices (IMD)
IMD-4: Helmholtz-Institut Münster
Forschungszentrum Jülich
Corrensstraße 46, D-48149 Münster, Germany

While post-synthesis processing steps are applied very frequently in the preparation of solid-state batteries, little is known about how exactly the processing step does influence the properties of the solid electrolyte. Recently, Schweiger et al. showed the effects of ball milling on $Li_{10}GeP_2S_{12}$ by nuclear magnetic resonance spectroscopy and found out that harsh ball milling leads to rapid amorphization with decreasing transport performance of the electrolyte.[27] Peng et al. used ball milling to obtain smaller particles of $Li_{5.5}PS_{4.5}Cl_{1.5}$ and thereby showed a decrease in the ionic conductivity.[28] Furthermore, changes in the microstructure of Li_6PS_5Cl due to wet milling affect the electrochemical stability against the lithium metal electrode.[29] Dewald et al. reported indications of lower coherence during the preparation of lithium-sulfur battery composites by ball milling.[30] In other cases where ball milling was used to synthesize solid-state electrolytes, clear changes of the local structure are observed.[31] While these results demonstrate that post-synthesis processing is decisive for the final properties of the solid electrolyte, questions about the actual processes occurring during milling remain open: What are the stresses acting on the solid electrolyte during milling? How do they affect the local structure, the crystallinity and the transport properties of the solid electrolyte? And what influence do the different processing parameters such as the processing method, the milling frequency, the milling time and the grinding media size have on the properties of the electrolyte and final cathode composite?

Inspired by the questions raised by these observations, we performed a systematic study on the effects of post-synthesis processing on the structure and transport properties of $Li_{5.5}PS_{4.5}Cl_{1.5}$. Investigating the crystallinity and local structure by X-ray diffraction (XRD), X-ray pair distribution function (XPDF) and neutron pair distribution function (NPDF) analyses as well as nuclear magnetic resonance (NMR) spectroscopy, shows that ball milling clearly decreases the crystallite size while increased disorder in the local structure can be observed. Scanning electron microscopy and laser diffraction reveal smaller particle sizes in processed samples compared to pristine ones. These changes are partly reversible as annealed samples show. By

© 2024 The Author(s). Advanced Energy Materials published by Wiley-VCH GmbH

16146840, 2025, 5, Downloaded from https://advanced.onlinelibrary.wiley.com/doi/10.1002/aenm.202403291 by Forschungszentrum Jülich GmbH Research Center, Wiley Online Library on [16/07/2025]. See the Terms and Conditions (https://onlinelibrary.wiley.com/terms-and-conditions) on Wiley Online Library for rules of use; OA articles are governed by the applicable Creative Commons License

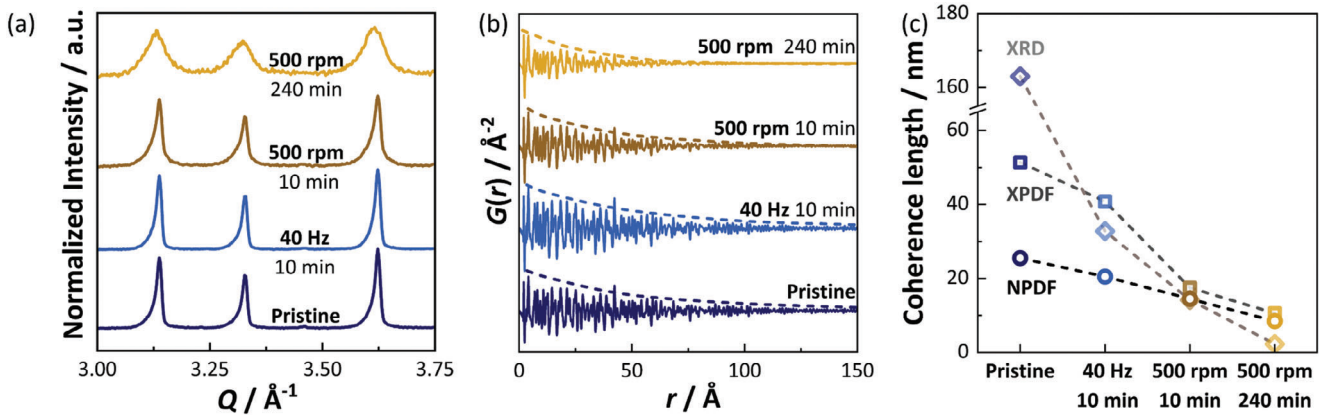


Figure 2. a) X-ray diffractogram of $Li_{5.5}PS_{4.5}Cl_{1.5}$ processed with 5 mm grinding media at different processing conditions demonstrates the broadening of the reflections with increasing ball milling time. b) The long-range neutron pair distribution function data shows faster decay of G(r) for the ball milled samples that was fit to extract coherence lengths. c) Extracted coherence lengths by small box modeling of NPDF and XPDF data and crystallite size from Rietveld refinement of the X-ray diffraction data.

performing discrete element simulations, differences in the specific energy input are revealed as major factor for the observed changes of the electrolyte for the first time. While the decrease in crystallinity with increasing energy input leads to reduced ionic conductivities, the smaller particles lead to lower tortuosity in cathode composites and better performance in solid state batteries. Due to these two opposite trends, short times of ball milling leads to the best capacities in solid-state battery half-cells. This work shows how important the influence of post processing composites is on the solid-state battery performance, an often-overlooked aspect in the research for improvement of solid electrolytes and solid-state batteries.

2. Results and Discussion

2.1. Effects on Crystallinity and Local Structure

In order to investigate the effect of different processing methods on the solid electrolytes, one large batch of $Li_{5.5}PS_{4.5}Cl_{1.5}$ was prepared via a modified route of a previously reported solid-state synthesis.[20] Rietveld refinement confirms the successful synthesis of the nearly phase pure solid electrolyte, only a minor LiCl phase fraction ≈1 wt.% can be found (Figure S1, Supporting Information). This batch was split into groups that were processed at three different conditions resembling the typical conditions of solid-state battery preparation. One part was treated in a frequency ball mill at 40 Hz for 10 min and another part was processed in a planetary ball mill for 240 min to resemble the standard conditions for the preparation of lithium sulfur solid state batteries.[32] A third part was processed at 500 rpm for 10 min to compare both methods. For all methods grinding media with a size of 5 mm was used. To study the effect of the processing on the crystal structure of the material, X-ray diffraction was carried out. For all samples, the diffraction pattern (Figure S2, Supporting Information) and diffraction peak position did not change significantly showing that the overall symmetry and crystal structure is retained. However, for the samples processed in the planetary ball mill diffraction peak broadening can be observed, most pronounced after four hours of processing (**Figure 2a**). This broadening indicates lower crystallinity and the presence of internal strain. Simultaneously, the increase of a broad background with the ball milling shows increased diffuse scattering and potentially lower coherence.

In addition to the diffraction data, complementary NPDF and XPDF analyses were performed to study the local structure of the materials. For a PDF analysis, the total scattering of the sample is measured over a large *Q*-range and a histogram of atom-atom distances is obtained via Fourier transformation. The large *r*-range of the NPDF of the differently processed samples (Figure 2b) reveals differences in the coherence length. While the NPDF of the pristine sample and the one processed in the frequency ball mill at 40 Hz still show clear signals above 100 Å, the samples milled at 500 rpm exhibit a faster decay in intensity. A similar decay for the samples processed at 500 rpm can be observed in the XPDF data (Figure S3, Supporting Information). Small box modeling with a spherical domain model allows to fit the decay of neutron and X-ray PDF by an envelope function and gives a quantitative estimation of the coherence length, i.e., the mean size of crystalline domains.[33] For the Bragg diffraction data, Rietveld refinement is used to extract the crystallite size and strain contribution of the peak broadening.[34] The induced strain is further analyzed by the Williamson-Hall method[35] on X-ray Bragg data measured on a copper diffractometer. The coherence lengths extracted by the described methods from NPDF and XPDF as well as Rietveld refinement are displayed in Figure 2c. All methods show the same relative reduction in the coherence length of $Li_{5.5}PS_{4.5}Cl_{1.5}$ with processing, especially when using the planetary ball mill. The extracted absolute values differ mostly for the pristine sample. With higher crystallite sizes the inaccuracy of the methods drastically increases leading to this spread for the pristine sample.[36] In addition to the decrease in crystallinity, the Williamson-Hall analyses also show an increase in internal strain for the samples that were processed in the planetary ball mill (Figure S4, Supporting Information). The strain values obtained by Rietveld refinement exhibit the same trend as the Williamson–Hall analyses and only differ in the proportionality factor (Figure S5, Supporting Information).

© 2024 The Author(s). Advanced Energy Materials published by Wiley-VCH GmbH

16146840, 2025, 5, Downloaded from https://advanced.onlinelibrary.wiley.com/doi/10.1002/aenm.202403291 by Forschungszentrum Jülich GmbH Research Center, Wiley Online Library on [16/07/2025]. See the Terms and Conditions (https://onlinelibrary.wiley.com/terms-and-conditions) on Wiley Online Library for rules of use; OA articles are governed by the applicable Creative Commons License

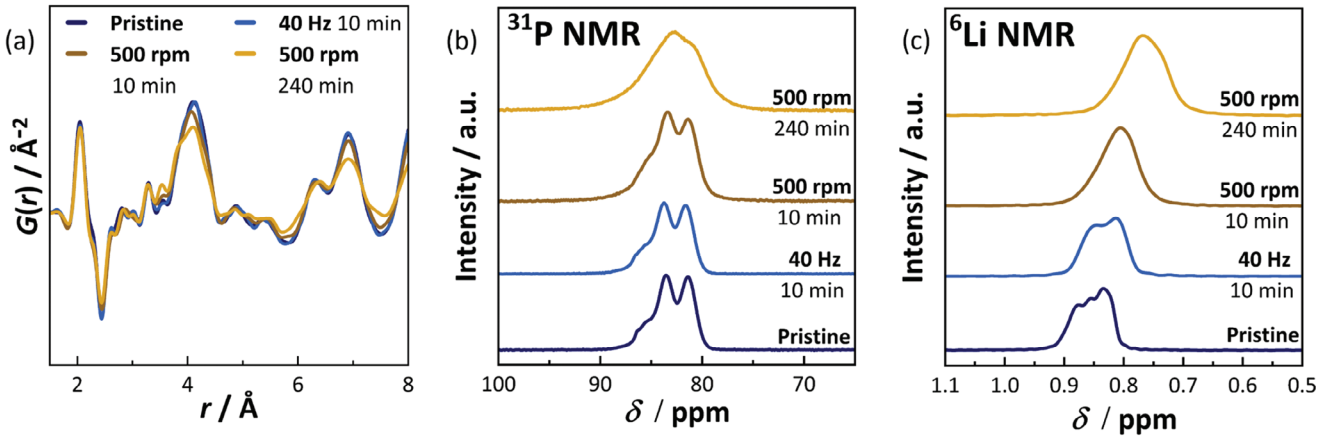


Figure 3. a) Broadening of peaks and lower maximum intensity above 4 Å in the NPDF of samples milled at 500 rpm reveals increased disorder in the local structure. b) ^{31}P MAS NMR and c) ^{6}Li MAS NMR spectra of pristine and processed $Li_{5.5}PS_{4.5}Cl_{1.5}$ show broadened resonances for the sample milled for four hours.

While the decay in intensity at higher atom – atom distances shows the difference in coherence length, the low *r* region of the NPDF (**Figure 3a**) gives information about the local structure. The positive peak at 2.04 Å corresponds to the P—S bond in the PS_4^{3-} unit, while the one at 2.44 Å corresponds to the closest Li^+-Cl^-/S^{2-}(4*d*) and is negative due to the negative neutron scattering length of ^{7}Li. These first peaks do not change for the differently processed samples showing that the rigid PS_4^{3-} polyanion and the first coordination sphere is not affected by ball milling. However, peaks at higher *r* broaden for the samples processed at 500 rpm with a lower maximum intensity indicating increased disorder in higher coordination spheres. The increased disorder correlates with the loss in crystallinity and reduced coherence length. Comparison of the NPDF transformed at different Q_{max} values confirms that the observed broadening is not caused by transformation artefacts but can be assigned to structural changes (Figure S6, Supporting Information). Small-box modeling of the pristine NPDF (Figure S7a, Supporting Information) by the cubic structural model results in a deviation between observed and calculated *G*(*r*) ≈4 Å. Schlenker et al. observed for the X-ray PDF of Li_6PS_5Cl discrepancies from the cubic structural model between 3 and 4.5 Å that could be fitted by a tilting of the PS_4^{3-} polyanions in a monoclinic model.[37] Based on the cubic model of $Li_{5.5}PS_{4.5}Cl_{1.5}$ a similar monoclinic model with *Cm* symmetry and rotationally disordered PS_4^{3-} polyanions was used to fit the neutron PDF data (Figure S8a,b, Supporting Information). For the pristine sample, this model (Figure S8c, Supporting Information) results in slightly better fit residuals and in a lower atomic displacement parameter for the PS_4^{3-} polyanion (Table S6, Supporting Information). As this result may indicate the presence of tilted polyanions in the local structure of pristine $Li_{5.5}PS_{4.5}Cl_{1.5}$, it leads to the hypothesis that an increase in rotational disorder of PS_4^{3-} polyanions is one of the reasons for the broadened peaks at 500 rpm. However, refining only the rotational disorder in the small box model did not fit the broadening of signals in the ball milled sample. The PDF of the samples processed at 500 rpm could only be fitted with high atomic displacement parameters for all atoms, demonstrating the induced disorder in the local structure. Similar broadening in the XPDF (Figure S9, Supporting Information) is observed that further shows increased disorder in the local structure for samples processed in the planetary ball mill.

^{31}P and ^{6}Li magic angle spinning (MAS) NMR measurements help to gain further information about the disorder in the local structure observed in PDF. Due to the Cl^-/S^{2-} disorder on the Wyckoff 4*d* position, each PS_4^{3-} polyanion can have five different combinations of ions on the four nearest Wyckoff 4*d* positions as reported for the structurally similar Li_6PS_5Br.[38] These different coordination possibilities lead to the line splitting observed in ^{31}P NMR (Figure 3b) of pristine $Li_{5.5}PS_{4.5}Cl_{1.5}$. For the sample milled at 500 rpm for 240 min, the splitting is not observable anymore while the center of the overall NMR line does not shift. This broadened NMR signal shows a wide distribution of inequivalent coordination environments of the PS_4^{3-} polyanions. In the ^{6}Li NMR spectra, a similar trend can be observed. The pristine sample (Figure 3c) reveals a signal that is composed of at least three different lines corresponding to different Li^+ positions and Wyckoff 4*d* environments. In the samples milled at 500 rpm, only a single broad line is visible clearly pointing to increased disorder in the Li^+ coordination environment. A slight shift toward higher fields may indicate small changes in the local environment of Li^+. High-resolution NMR data corroborate the results from the PDF analyses of increased disorder in the local structure although the exact structural disorder remains difficult to deconvolute.

Since the lithium argyrodites are polycrystalline materials, the crystallite size does not equal the size of secondary particles. Scanning electron micrographs (Figure S10a, Supporting Information) show for the pristine sample a distribution of polydisperse particles with large particles of over 100 µm in diameter. This particle size decreases to less than 50 µm after processing in the frequency ball mill. Higher magnification reveals the presence of agglomerates, consisting of smaller particles. For the samples processed at 500 rpm in the planetary ball mill the smallest individual particles are observed. The cumulative particle size distributions of the ultrasonicated samples (Figure S10b, Supporting Information) confirm the large number of particles with a diameter over 50 µm in the pristine sample. After 10 min of

© 2024 The Author(s). Advanced Energy Materials published by Wiley-VCH GmbH

16146840, 2025, 5, Downloaded from https://advanced.onlinelibrary.wiley.com/doi/10.1002/aenm.202403291 by Forschungszentrum Jülich GmbH Research Center, Wiley Online Library on [16/07/2025]. See the Terms and Conditions (https://onlinelibrary.wiley.com/terms-and-conditions) on Wiley Online Library for rules of use; OA articles are governed by the applicable Creative Commons License

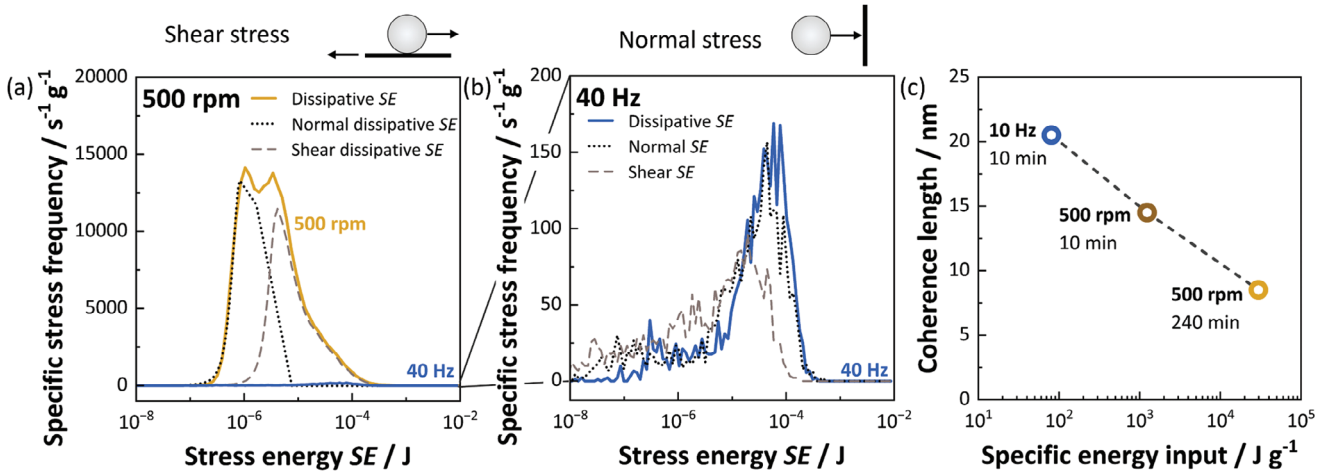


Figure 4. a) Specific stress frequency against dissipation stress energy curve obtained by discrete element method for the 5 mm grinding media. The dotted line represents the calculated normal component and the dashed line the shear components of the dissipative stress energy distribution. b) Zoom-in for the frequency ball mill showing the normal components have the dominant impact in the milling process. c) Calculated specific energy input during the different ball milling procedures correlates with the coherence lengths determined by NPDF.

milling at 40 Hz, a broad particle size distribution with a median particle size of 10 µm is observed. The samples processed at 500 rpm exhibit a narrower distribution with a smaller median particle size of ≈ 5 µm. There is only a slight further decrease in particle size with longer milling time or stress number, respectively, which indicates that a minimum of particle size for these milling conditions is reached.

2.2. Discrete Element Simulations of Milling Conditions

Processing in the planetary ball mill at 500 rpm leads to a stronger reduction in crystallite and particle size as well as more disorder in the local structure compared to processing in the frequency ball mill. To better understand these observed differences between the two milling methods, simulations are performed using a discrete element method. The Hertz–Mindlin contact model[39,40] and the linear spring rolling limit model were used to determine the forces occurring when the grinding media collide. The stress energy SE and its mean value $\overline{SE}$ describe the energy transferred involved within an impact. Here we can determine the entire energy in either normal or tangential direction (shear energy) of the relative media motion, as well as the plastic energy in both directions named dissipative energy.[41] By assuming that the stressed product mass is independent of operating conditions, the stress energy is directly proportional to the stress intensity, which relates the stress energy to the stressed product mass.[42] The specific stress frequency SF_m (frequency of grinding media collisions per mass of product in mill) in the planetary ball mill (**Figure 4a**) is larger and the stress energy distribution is significantly broader when compared to the frequency ball mill. This means that more collisions occur in the planetary ball mill per product mass for a certain process time, and a broad distribution of high-energy and low-energy collisions are present. Collisions of higher energy have a high shear component, which can be explained by the rolling of the grinding media on the grinding chamber wall, while the lower dissipative stress energies mainly stem from the normal component. In contrast, the frequency ball mill (Figure 4b) predominantly shows collisions with a high normal proportion, which is because the grinding media oscillate primarily from lower wall to upper wall and back, thereby stressing above all the material between the grinding media and the grinding chamber. The higher specific stress frequency of sufficient stress energies in the planetary ball mill leads to faster comminution resulting in smaller particles. In particular, the high shear fractions and the grinding effect of the grinding media rolling on the wall ensure an additional comminution effect compared to the frequency ball mill.

Figure 4c shows the specific energies, that act on the solid electrolyte during the milling process, for the three different milling conditions with 5 mm grinding media and compares them to the determined crystallite sizes from neutron pair distribution function analyses. For an in-depth discussion on the calculated specific energies, we refer to the Experimental Section. In short, the specific energy represents the product of the stress energy, the specific stress frequency and the time of the milling process. With increasing specific energy input, the coherence and thus the crystallinity of the solid electrolyte decreases. This can be attributed to the increasing number of stress events on the material with increasing milling time. In particular, the broad stress energy distribution present in the planetary ball mill with a high number of collisions causes a strong decrease in the crystallinity of the solid electrolyte and increased disorder in the local structure. Furthermore, the particle size exhibits a higher decrease in the planetary ball mill than in the frequency ball mill. As the reduction in particle size correlates with the total energy input, larger milling times in the frequency ball mill should further reduce the particle size. However, at a certain point the effect of caking, i.e., the aggregation of powder on the walls of the milling cup, will mitigate further comminution of (secondary) particles. To further explore the influence of the milling conditions on the stressing and overall energy input, various parameters such as carrying the milling frequency and milling media size were simulated. These data can be found in the Supporting Information,

© 2024 The Author(s). Advanced Energy Materials published by Wiley-VCH GmbH

16146840, 2025, 5, Downloaded from https://advanced.onlinelibrary.wiley.com/doi/10.1002/aenm.202403291 by Forschungszentrum Jülich GmbH Research Center, Wiley Online Library on [16/07/2025]. See the Terms and Conditions (https://onlinelibrary.wiley.com/terms-and-conditions) on Wiley Online Library for rules of use; OA articles are governed by the applicable Creative Commons License

overall showing that the stress energy increases with increasing milling speed or milling frequency (Figure S11, Supporting Information), whereas a stronger influence of an increasing grinding media mass on the stress energy was found in the frequency mill (Figure S12, Supporting Information).

To correlate the simulation results with additional experimental data, the argyrodite was processed with a different grinding media size of 3 mm. This results in higher specific stress frequencies with a lower stress energy in both methods during processing. The structural investigation (Figure S13, Supporting Information) reveals similar results with only slight deviations to the samples processed with 5 mm grinding media within each set of parameters indicating that the similar specific power has a dominant influence.

2.3. Effects on Ionic Transport

To understand the effects of the structural changes on the ionic transport, ^{7}Li spin-lattice relaxation (SLR) NMR measurements and electrochemical impedance spectroscopy are combined to probe the local and long-range transport. The analysis of local diffusion of mobile ions by ^{7}Li SLR NMR is based on the relaxation model of Bloembergen, Purcell, and Pound (BPP).[43] Diffusion-controlled SLR rates T_1^{-1} of the mobile ions reach their maximum when the motional correlation rate reach the order of the angular Larmor frequency. The correlation rate is proportional to the ionic jump rate within a factor of 2. Analyzing the T_1^{-1} relaxation rates as a function of temperature therefore allows the determination of jump rates and activation energies of the elementary diffusion processes. The Arrhenius plots of the diffusion-induced ^{7}Li NMR T_1^{-1} relaxation rates of the pristine and processed samples are shown in **Figure 5a**. Solid lines represent the analysis according to a modified BPP model, which allows the slope of the low-temperature flank to take values lower than that on the high-T side.[44,45] From the temperature at the rate maximum T_{max}, a jump rate of 7×10^8 s^{-1} for the pristine sample can be estimated. No significant changes of T_{max} are observed between pristine $Li_{5.5}PS_{4.5}Cl_{1.5}$ and the sample processed at 40 Hz. Compared to the pristine one, the peaks referring to the samples treated in the planetary ball mill are, however, slightly shifted toward higher temperatures. These small shifts reveal that the (local) Li^+ diffusivity in the solid electrolyte has slightly decreased after processing at 500 rpm.

To further study the long-range ionic transport, temperature-dependent potentiostatic impedance spectroscopy was carried out. The impedance spectra at −40 °C can be modeled by a parallel resistor and constant phase element in series with a constant phase element (Figure 5b). No grain boundary contributions can be deconvoluted from bulk transport that is often observed for lithium argyrodites.[46] At room temperature and above only the blocking electrode contribution is detected for the pristine sample due to the high conductivity of the electrolyte (Figure S14a, Supporting Information). The fits result in a bulk conductivity of 6.8(2) mS · cm^{-1} at room temperature for the pristine $Li_{5.5}PS_{4.5}Cl_{1.5}$ that is in the range of previously reported values.[20] The conductivity of the sample processed in the frequency ball mill lies within the error margin. In contrast, the samples milled at 500 rpm show a major decrease in ionic conductivity with 5.3(2) mS · cm^{-1} after 10 min and 2.8(2) mS · cm^{-1} after 240 min. With the decrease in crystallinity and particle size in the longest milled sample one might expect larger contributions of grain boundary resistances, however, even at −100 °C (Figure S14b, Supporting Information) only one process is detected and bulk and grain boundary transport cannot be deconvoluted. When analysing the influence of different grinding media sizes (Figure S14c, Supporting Information), the 3 mm grinding media exhibit slightly lower conductivities than the 5 mm grinding media within the same milling conditions. Once the necessary energy for comminution of crystallites is reached, the higher number of collisions with 3 mm grinding media might cause further reduction in ionic conductivity. However, the differences are close to the uncertainty of the measurement procedure.[47] From the temperature-dependence of the ionic conductivity the activation energies were determined via Arrhenius plots (Figure S14d, Supporting Information). The activation energy of pristine $Li_{5.5}PS_{4.5}Cl_{1.5}$ of 0.38 eV aligns with reported literature values[20] and does not change for the processed samples. Figure 5c compares these values to the activation energies obtained from the ^{7}Li relaxometry data. The asymmetry in the fitted BPP functions allows to extract activation energies of the long-range transport from the high-temperature side of the rate peak with values between 0.28 and 0.30 eV that are near the values of those obtained by impedance spectroscopy. The activation energies on the low temperature flank low energy barriers for fast but localized ion diffusion in argyrodites and are in the range of 0.12 – 0.13 eV for all samples. From the combined measurements it can be concluded that all determined activation energies do not significantly change with processing. Comparing the ionic conductivities with the coherence lengths determined by neutron PDF analyses (Figure 5d) shows a clear correlation between structural coherence and ionic conductivity. With increasing ball milling energy and increasing stress number, the coherence length and ionic conductivity of $Li_{5.5}PS_{4.5}Cl_{1.5}$ both decrease. With a reduced coherence length, a decrease in the size of the crystallites is expected. The crystallites are likely to be embedded in an amorphous matrix as no grain boundary contributions could be resolved. With lower coherence, the long-range diffusion pathways might be interrupted leading to the decrease in ionic conductivity. The loss in coherence is partly reversible by annealing. When the sample processed at 500 rpm for 240 min is heated at the synthesis temperature of 450 °C for 48 h, less broadened reflections are obtained in the X-ray diffractogram (Figure S15, Supporting Information). The coherence length extracted by XPDF is increased, but does not reach the value of the pristine sample while agglomerates of small particles are still present. The ionic conductivity increases to a value of 5.3(2) mS · cm^{-1} in accordance with the increased structural coherence underlining the reversibility of the milling effects.

2.4. Effects on Cathode Composites

Since bulk ionic conductivity and particle size trend in opposite directions for the processed samples, an analysis of the effective ionic conductivity is helpful to assess the effects of processing on the performance of cathode composites. The effective ionic conductivity σ_{eff} is determined by the bulk ionic conductivity σ_{bulk},

© 2024 The Author(s). Advanced Energy Materials published by Wiley-VCH GmbH

16146840, 2025, 5, Downloaded from https://advanced.onlinelibrary.wiley.com/doi/10.1002/aenm.202403291 by Forschungszentrum Jülich GmbH Research Center, Wiley Online Library on [16/07/2025]. See the Terms and Conditions (https://onlinelibrary.wiley.com/terms-and-conditions) on Wiley Online Library for rules of use; OA articles are governed by the applicable Creative Commons License

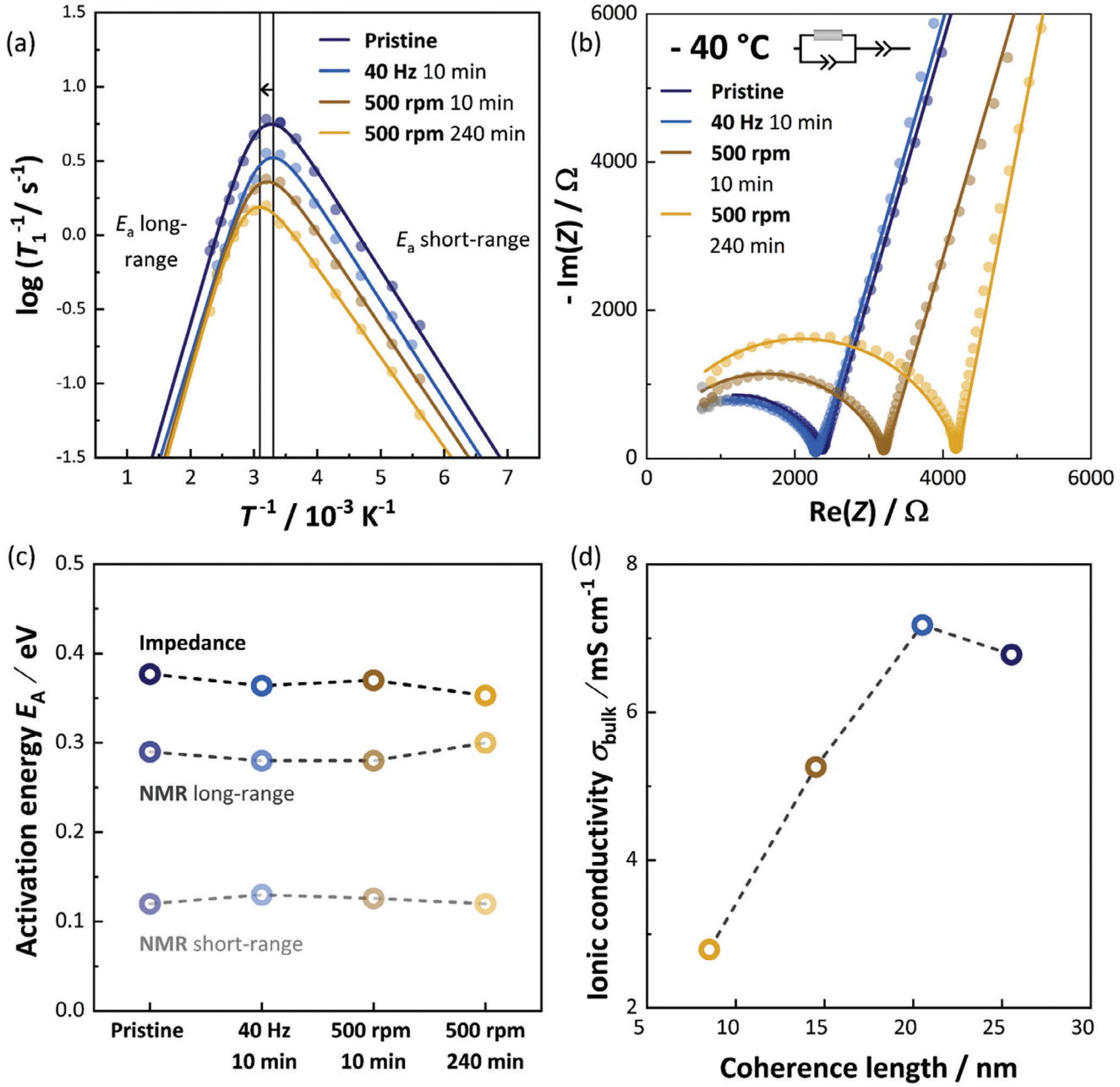


Figure 5. a) Diffusion-induced ^{7}Li SLR NMR rates reveal a shift of the peak maximum toward higher temperatures for the samples prepared by ball milling using planetary mills. These small shifts reveal a slightly decreased (local) Li^+ diffusivity in mechanically treated $Li_{5.5}PS_{4.5}Cl_{1.5}$. For clarity, the originally overlapping peaks were shifted down the y-axis; mechanical treatment does not significantly affect their amplitudes. b) Nyquist plots of processed $Li_{5.5}PS_{4.5}Cl_{1.5}$ determined from impedance spectroscopy in press cells at −40 °C. c) Comparison of activation energies determined by temperature-dependent impedance spectroscopy and ^{7}Li SLR NMR. All methods show activation energies within the uncertainty. d) The ionic conductivity of the differently processed samples correlates with the coherence lengths obtained by NPDF.

the volume fraction Φ_i of the conducting material in the composite and the tortuosity factor κ_i according to Equation 1.

$$\sigma_{eff} = \frac{\Phi_i}{\kappa_i} \times \sigma_{bulk} \quad (1)$$

The tortuosity factor plays a crucial role in the performance of the composite.[48] Recent studies showed how smaller particle sizes of the solid electrolyte lead to lower tortuosity and higher effective ionic conductivities.[21,49] Composites of the different samples with $LiNi_{0.83}Co_{0.11}Mn_{0.06}O_2$ (NCM811) were prepared and impedance spectroscopy was measured in symmetrical cells in electron-blocking configuration to obtain the effective ionic transport (Figure S16a, Supporting Information). The obtained impedance spectra result from convoluted contributions of ionic transport in the solid electrolyte, electronic transport in

© 2024 The Author(s). Advanced Energy Materials published by Wiley-VCH GmbH

16146840, 2025, 5, Downloaded from https://advanced.onlinelibrary.wiley.com/doi/10.1002/aenm.202403291 by Forschungszentrum Jülich GmbH Research Center, Wiley Online Library on [16/07/2025]. See the Terms and Conditions (https://onlinelibrary.wiley.com/terms-and-conditions) on Wiley Online Library for rules of use; OA articles are governed by the applicable Creative Commons License

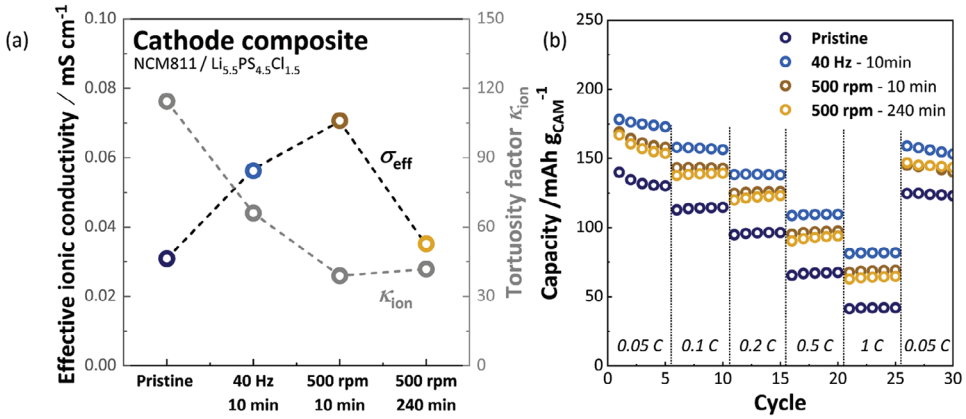


Figure 6. a) Measured effective ionic conductivities and calculated tortuosity factors of cathode composites of NCM811 and processed $Li_{5.5}PS_{4.5}Cl_{1.5}$. The samples that were processed at 500 rpm for ten minutes show the highest partial ionic conductivity and lowest tortuosity factor. b) Rate capability tests of the four composites reveal an improved performance for shortly processed samples.

the cathode active material as well as charge transfer at the interphase of both compounds. Therefore, a T-type transmission line model (Figure S16b, Supporting Information) was used to deconvolute the partial ionic and electronic conductivities according to Minnmann et al.[50]

The fitted Nyquist plots are displayed in Figure S17c (Supporting Information). The extracted effective ionic conductivities (**Figure 6**a) show a different trend to the ionic conductivities of the pure solid electrolytes. σ_{eff} increases from the pristine sample to the electrolyte processed at 40 Hz and reaches its maximum for the material that was milled at 500 rpm for 10 min. With the longer milling time of 240 min it decreases. From these effective ionic conductivities and the bulk ionic conductivities of the processed electrolytes (Figure 5d) the tortuosity factor κ_i of the four samples was determined. The tortuosity factor decreases with milling at 40 Hz and is the lowest after milling in the planetary ball mill where the sample milled for 10 and for 240 min exhibit nearly the same value. The lower tortuosity can also be seen in scanning electron micrographs of the composites (Figure S17, Supporting Information). This trend is highly correlated to the measured particle size distributions that corroborates that smaller particles lead to more effective ionic transport in the composite. The re-annealed sample exhibits a better effective ionic conductivity than the pristine and the longest milled sample (Figure S18, Supporting Information). While the particles in the annealed sample are still smaller than those of the pristine one leading to lower tortuosity, its bulk ionic conductivity is increased compared to the sample milled for 240 min.

The effect of the processed solid electrolytes on the rate-dependent cycling performance of solid-state batteries was investigated with the $Li_{5.5}PS_{4.5}Cl_{1.5}$/NCM811 cathode composites. The obtained discharge capacities at different C-rates are shown in Figure 6b. All samples exhibit a typical drop in the initial charge capacity, which is related to the loss of active lithium,[51] structural rearrangements, and contact loss.[52] The post processing that affects the microstructure and ionic partial transport affects the overall capacities, leading to higher attainable capacitites compared to using the pristine solid electrolyte. **Figure 7** schematically visualizes the two main effects that can be concluded for the processed $Li_{5.5}PS_{4.5}Cl_{1.5}$. Ball milling in the planetary ball mill leads to a continuous decrease in coherence length causing lower ionic conductivities in the pure solid electrolyte. Nevertheless, the milling decreases the particle size of the solid electrolytes. Mixed with cathode active material, the smaller electrolyte particles produce a composite with lower tortuosity factor and more effective transport pathways for Li^+ ions. For the shortly milled samples, the effect of a smaller particle size compensates the slight decrease in the bulk ionic conductivity resulting in higher effective ionic conductivity and, hence, better cell performance than the pristine sample. With a longer ball milling time of 240 minutes, particles become only slightly smaller while the coherence length is significantly further reduced. Hence, the effective ionic conductivity and cell performance decrease.

3. Conclusion

Using a multitude of experimental techniques allowed the deconvolution of the various effects that post-synthesis ball milling has on the solid electrolyte $Li_{5.5}PS_{4.5}Cl_{1.5}$. A combination of XRD, NPDF and XPDF shows a decrease in structural coherence and allowed the quantification of the crystallite size and straining occurring due to the processing. PDF analyses and MAS NMR spectroscopy both observed an increase in disorder in the local structure with long ball milling times. The decrease in crystallinity correlates with lower bulk ionic conductivities for samples processed in the planetary ball mill. Furthermore, ball milling reduces the particle size of the solid electrolyte. By annealing at 450 °C these observed changes were partly reversible. The smaller particles lead to lower tortuosity factors in the cathode composites seemingly counteracting the decrease in the ionic conductivity of the solid electrolyte itself. For short ball milling times, the lower tortuosity outweighs the reduction in ionic conductivity and therefore results in a better cell performance. With longer milling times the further decreasing coherence length leads to a drop in capacity that can be achieved. Discrete element simulations shed light into the acting stresses during the ball milling process. While in the frequency ball mill collision in normal direction have the major impact, a larger number of high energy shear stresses sum up to a much higher specific energy input in the planetary ball mill. Slightly lower ionic conductivities for smaller

© 2024 The Author(s). Advanced Energy Materials published by Wiley-VCH GmbH

16146840, 2025, 5, Downloaded from https://advanced.onlinelibrary.wiley.com/doi/10.1002/aenm.202403291 by Forschungszentrum Jülich GmbH Research Center, Wiley Online Library on [16/07/2025]. See the Terms and Conditions (https://onlinelibrary.wiley.com/terms-and-conditions) on Wiley Online Library for rules of use; OA articles are governed by the applicable Creative Commons License

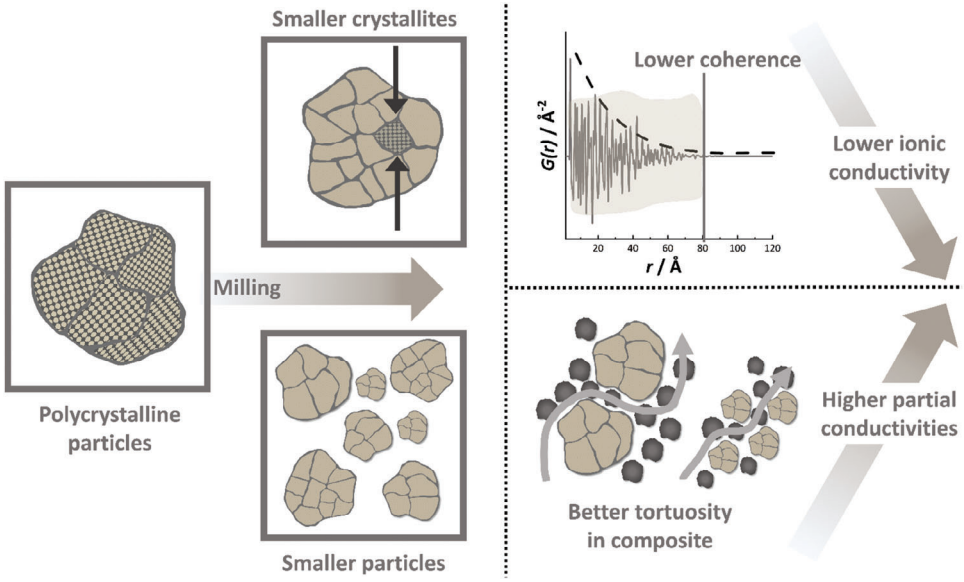


Figure 7. Schematic representation of the two main effects of ball milling on $Li_{5.5}PS_{4.5}Cl_{1.5}$. While smaller crystallites reduce the ionic conductivity of the pure solid electrolyte, the decrease in particle size leads to lower tortuosity and higher effective ionic conductivities in the composite at the same time.

grinding media indicate that the decrease in crystallinity is not only affected by the energy input but also the number of collisions. This improved understanding of the milling process can be a starting point for further optimization of the milling conditions to ensure small particles while mitigating the loss of structural coherence. This work demonstrates that optimizing the post synthesis processing of solid electrolytes plays a crucial role in improving the performance of solid-state batteries, an often overlooked or rarely mentioned influence.

4. Experimental Section

Solid-State Synthesis of $Li_{5.5}PS_{4.5}Cl_{1.5}$: Samples were prepared by a modified route of a previously reported synthesis.[20] The pristine electrolyte was synthesized by solid-state synthesis under inert conditions using stoichiometric amounts of Li_2S (Alfa-Aesar, 99.9%), P_2S_5 (Sigma–Aldrich, 99%) and LiCl (Alfa-Aesar, 99%). The LiCl was pre-treated in a Fritsch PULVERISETTE 7 planetary ball mill (4 h at 500 rpm in cycles of 10 min of milling with subsequent resting time of 10 min) and all precursors were ground in a mortar for 20 min, pressed into pellets and filled into carbon-coated quartz ampoules that were dried at 800 °C under dynamic vacuum for two hours. The ampoules were sealed under vacuum and placed into a horizontal tube furnace at 450 °C for 48 h after heating up with a rate of 100 °C per hour and left to cool down to room temperature. After the first annealing, the intermediate product was ground again for 20 min, pressed into pellets and heated a second time at 450 °C for 48 h in evacuated ampoules.

Post-Synthesis Processing: Frequency ball mill samples were processed in a Fritsch PULVERISETTE 23 at 40 Hz for 10 min, in batches of 200 mg of pristine $Li_{5.5}PS_{4.5}Cl_{1.5}$ with 2 g of grinding media (zirconium oxide, 3 mm or 5 mm diameter). For the samples in the planetary ball mill, 1 g of pristine electrolyte was added to 10 g of grinding media (zirconium oxide, 3 mm or 5 mm) in an 80 mL zirconium oxide ball mill cup. The material was processed in a Fritsch PULVERISETTE 7 at 500 rpm for 10 min. For the long processing time, 24 cycles of 10 min ball milling at 500 rpm with subsequential pauses of 10 min were applied.

X-Ray Diffraction and Williamson-Hall Analyses: The X-ray diffraction data were recorded using a Stoe STADI P diffractometer (Mo $K_{\alpha 1}$ radiation: $\lambda = 0.70930$ Å, Ge (111) monochromator) in Debye-Scherrer geometry equipped with a Dectris MYTHEN2 1K detector. The samples were measured in sealed glass capillaries over a 2θ-range of 4 – 45° with a scanning rate of 1° per minute. Phase analyses and Rietveld refinements were carried out using TOPAS academics V7.[53] R_{wp}, R_{exp}, and goodness of fit (*gof*) were used as fit indicators to assess the quality of the refinement. The profile was refined by 1) a scale factor, 2) 6 free background coefficients of a Chebyshev polynomial function, 3) peak shape parameters of a modified Thompson–Cox–Hastings pseudo-Voigt function,[54] 4) a full axial model to account for the asymmetry of the peak due to axial divergence as described by Cheary et al.,[55] 5) a zero point offset, 6) the lattice parameters. With fixed profile, 7) the fractional atomic coordinates and subsequently 8) isotropic atomic displacement parameters were fit. The profile of a Nist c660 LaB_6 standard measurement was fitted by a Thompson–Cox–Hastings pseudo-Voigt function and the fixed profile was used to refine influence of strain and crystallite size in TOPAS academics V7.

Due to better peak separation and lower asymmetry, X-ray diffraction data for Williamson-Hall analyses were collected on a Stoe STADI P diffractometer with Cu $K_{\alpha 1}$ radiation ($\lambda = 0.70930$ Å) and Ge 111 monochromator in Debye-Scherrer geometry with a MYTHEN 1K detector. Sealed glass capillaries were measured in moving mode over a 2θ-range 10 – 70° with a step size of 3° and a measurement time of 360 s per step. The Williamson-Hall method was used to deconvolute the contributions of internal strain and crystallite size. The integral breadth β of the Bragg peaks was determined by fitting each Bragg peak with a pseudo-Voigt function. From the Williamson–Hall equation:[35]

$$\beta\cos\theta = C\epsilon\sin\theta + \frac{K\lambda}{d} \quad (2)$$

with the proportionality factors C and K the contributions of internal strain ϵ and crystallite size d were determined.

Neutron Pair Distribution Function (NPDF) and X-Ray Pair Distribution Function (XPDF) Analyses: Neutron total scattering data were collected at 100 and 297 K using the Nanoscale Ordered Materials Diffractometer (NOMAD) at the Spallation Neutron Source (SNS). The samples were

© 2024 The Author(s). Advanced Energy Materials published by Wiley-VCH GmbH

16146840, 2025, 5, Downloaded from https://advanced.onlinelibrary.wiley.com/doi/10.1002/aenm.202403291 by Forschungszentrum Jülich GmbH Research Center, Wiley Online Library on [16/07/2025]. See the Terms and Conditions (https://onlinelibrary.wiley.com/terms-and-conditions) on Wiley Online Library for rules of use; OA articles are governed by the applicable Creative Commons License

loaded into a 3 mm quartz capillary and then sealed in a glovebox using epoxy resin. Software available at the beamline was used to calculate the NPDF with a Q_{max} of 28 Å^{-1}. The normalized scattering intensity $I(Q)$ was produced by subtracting background signal from the event-based data followed by vanadium normalization. An arbitrary scaling factor was applied to produce structure factor $S(Q)$, so that $\lim_{Q\to\infty} S(Q) = 1$. A Fourier filter was applied to produce the expected behavior, $\lim_{r\to 0} G(r) = -4\pi r\rho$, at the limit of the reduced pair distribution function $G(r)$.

X-ray total scattering data were recorded using a Stoe STADI P diffractometer (Ag $K_{\alpha 1}$ radiation: $\lambda = 0.55941$ Å, Ge 111 monochromator) in Debye-Scherrer geometry with four Dectris MYTHEN2 1K detectors as described by Thomae et al.[56] The samples were measured in sealed glass capillaries over a Q-range of 0.8–20.5 Å^{-1} for 24 h. Data reduction was carried out using PDFgetX3 with a Q-range cutoff of $Q_{max} = 15$ Å^{-1}.[57]

Small box modeling of the NPDF was performed over a r range of 1.8 to 10 Å using PDFgui.[58] Subsequently, the 1) scale factor, 2) correlated motion factor, 3) lattice parameters, 4) atomic positions, 5) isotropic atomic displacement parameters, and 6) occupancies were refined using the cubic Rietveld refinement structure as starting model. To refine a potential rotation of PS_4^{3-} polyanions, the cubic structure obtained by small box modeling of the pristine sample was transformed into *Cm* symmetry with a $\sqrt{a}$ modulation using the ISODISTORT software[59] and the S13-S16 sulfur positions and atomic displacement parameters were refined while fixing the other structural parameters. To obtain coherence lengths, the decay of the NPDF and XPDF over a r range from 1.8 to 120 Å was fitted in TOPAS academics V7 with an envelope function by a spherical diameter model. The instrumental resolution parameters Q_{broad} and Q_{damp} were determined from a reference measurement of crystalline silicon.

Nuclear Magnetic Resonance (NMR) Spectroscopy: ^{6}Li and ^{31}P magic angle spinning (MAS) spectra were recorded on a Bruker III Avance 500 NMR spectrometer connected to an ultrashielded 500 MHz magnet with a nominal field of 11.74 T resulting in resonance frequencies of 73.6 MHz for ^{6}Li and 130 MHz for ^{31}P, respectively. Chemical shifts reported refer to those of ^{6}Li in CH_3COOLi (0.1 ppm when referenced to (LiCl)) and ^{31}P in H_3PO_4 (0 ppm) measured with the help of solid $CaHPO_4$ serving as a second reference. Prior to the measurements, the polycrystalline powder samples were packed into 2.5 mm MAS rotors made of ZrO_2. The ^{6}Li and ^{31}P NMR measurements were performed at a spinning speed of 25 kHz and at 303 K (N_2 bearing gas). ^{6}Li NMR spectra were recorded with a single-pulse sequence applying a pulse length of 5.0 µs at a power level of 100 W. 32 scans were accumulated with a recycle delay of 50 s. For ^{31}P, a pulse length of 1.48 µs was applied (180 W). 64 scans were accumulated and recorded with a recycle delay of 20 s, to obtain the ^{31}P free induction decays (FIDs). Fourier transformation directly yields the NMR spectra without further manipulation of the time-domain data. For the ^{7}Li static, that is, non-MAS, NMR measurements, the samples were sealed under vacuum in Duran glass tubes (4 cm in length, 3 mm in inner diameter). Variable-temperature spin-lattice relaxation (SLR) experiments in the laboratory frame ($1/T_1$) were performed covering a temperature range from 178 K to 413 K. The time-domain experiments were carried out with a Bruker Avance III spectrometer connected to an ultrashielded 300 MHz magnet with a nominal magnetic field of 7 T. The Larmor frequency of this field corresponds to 116 MHz for ^{7}Li. Diffusion-induced SLR rates were measured with the classical saturation recovery pulse sequence.[60] The $\pi/2$ pulse lengths, slightly depending on temperature, ranged from 2.07 to 2.75 µs if a power level of 200 W was used. To extract the rates $T_1^{-1}(1/T)$, describing the recovery of longitudinal magnetization M_z, along the z direction, the area under the corresponding FIDs was plotted against the waiting time t_d. The resulting magnetization transients $M_z(t_d)$ were analyzed with single, but stretched exponential functions $M_z(t_d) \propto 1-\exp(-t_d/T_1)^{\gamma}$ with the stretching parameter γ taking values from 0.8 and 1.0.

Scanning Electron Microscopy: For sample preparation, solid electrolyte powder was attached to the sample holder with double-sided carbon tape. For measurements of cathode composites, 30 mg of the prepared composite were pressed with a uniaxial pressure of 374 MPa for 3 min and the pellet was placed on the sample holder with double-sided carbon tape. The holders were coated with a layer of gold by a Cressington Sputter Coater with an applied current of 40 mA for 30 s under reduced pressure of 0.05 mbar. Scanning electron microscopy was performed at a Carl ZeissAURIGA CrossBeam working station (accelerating voltage of 3 kV) with an In-lens detector.

Particle Size Distribution: The particle size distribution was determined by a Sympatec Helos instrument. A small amount of the powder was placed in a small snapper with xylene and then ultrasonicated with an ultrasonic finger for ≈15 min. The suspension was then injected into the measurement cuvette outside the glovebox for the measurement and stirred again by hand. The measurement cuvette contained a solution of 99 wt.% xylene and 1 wt.% oppanol, which was added to increase the viscosity of the solution to prevent large particles from sedimenting. Six measurements of ten seconds were recorded for each sample.

Discrete Element Method Simulations: The simulation set-up of the frequency ball mill and the set-up of the planetary ball mill can be seen in Figure S19 (Supporting Information). For the simulation of the frequency ball mill, 2 g of grinding media were inserted, and the frequency ball mill was moved with a frequency of 40 Hz and a peak to peak amplitude of 9 mm in translational direction for 5.5 s. The properties of the grinding media (zirconia, see Table S7, Supporting Information) were taken from the manufacturer's specifications and previous calibration tests assuming that $Li_{5.5}PS_{4.5}Cl_{1.5}$ behaves congruently with Li_6PS_5Br.[41,61] The grinding media and the grinding chamber were calibrated as if the surface was covered with material. This enables a realistic simulation of the acting stress energies $\overline{SE}$ while reducing the simulation times. Since a stationary state was reached after ≈1 s mixing time, the power data as well as the grinding media-related stress energies $\overline{SE}_{GM}$ and stress numbers SN between 1 s and 5.5 s were evaluated.[62] The grinding media sizes varied between 3, 5 and 10 mm. For the simulation of the planetary ball mill, 10 g of grinding media were inserted into the simulation domain and the simulation was run for 5.5 s congruent to the simulation of the frequency ball mill. The rotational speed of the sun was set to $n_{sun} = 500$ rpm, which leads to a rotational speed of the grinding chamber of $n_{GC} = -1000$ rpm with a speed ratio of $k = -2$. The forces acting on the grinding media were determined by the Hertz–Mindlin contact model.[39,40] The collision powers P_i^{α} per grinding media i per output interval $\Delta t_{out} = 0.5$ ms determined from the forces were converted into collision-based mean stress energies $\overline{SE}_{GM}$ similar to Frankenberg et al.[62] For this purpose, the grinding media-related specific power data per time interval Δt_{out} were exported and divided by the collision frequency $\overline{c_i}$.

$$\overline{SE}_{GM}^{\alpha} = \frac{P_i^{\alpha}}{\overline{c_i}} = \frac{\sum_{k=1}^{N_{k,i}} W_k^{\alpha}}{\Delta t_{out}} \times \frac{\Delta t_{out}}{N_{k,i}} = \frac{\sum_{k=1}^{N_{k,i}} W_k^{\alpha}}{N_{k,i}} \quad (3)$$

$N_{k,i}$ stands for the number of collisions of grinding media i in the time interval Δt_{out}, W_k^{α} for the collision energy calculated from the contact forces, and α denotes the differentiation of the collisions into normal collision energy, tangential collision energy and dissipation collision energy. Moreover, the stress frequency was numerically determined and related to the product mass in the specific mill. Specific stress frequency – stress energy curves ($SF_m - SE$) of the two different processing methods were generated according to Hofer et al.[41] The $SF_m - SE$ curves were used to determine the total specific number of collisions occurring per second of mixing and mass of product, which is referred to below as the specific stress frequency SF_m. By multiplying the specific stress frequency with the overall mixing time t_{mixing}, the so-called specific stress number SN_m results. The specific energy acting on the solid electrolyte or cathode material mixture, E_m, is then determined from the mean stress energy $\overline{SE}$ as well as SF_m and overall mixing time t_{mixing} or SN_m according to Equation 4.[40]

$$E_m = \overline{SE} \times SF_m \times t_{mixing} = \overline{SE} \times SN_m \quad (4)$$

Electrochemical Analyses: All electrochemical measurements were performed in customized press cells consisting of a brass casing with PEEK insets and stain-less steel stamps of 10 mm diameter as electrodes.[63] An aluminum frame with a torque of 10 Nm applied a pressure of 50 MPa

© 2024 The Author(s). Advanced Energy Materials published by Wiley-VCH GmbH

16146840, 2025, 5, Downloaded from https://advanced.onlinelibrary.wiley.com/doi/10.1002/aenm.202403291 by Forschungszentrum Jülich GmbH Research Center, Wiley Online Library on [16/07/2025]. See the Terms and Conditions (https://onlinelibrary.wiley.com/terms-and-conditions) on Wiley Online Library for rules of use; OA articles are governed by the applicable Creative Commons License

during the measurements. For potentiostatic electrochemical impedance spectroscopy measurements of pure electrolytes, the cells were filled with 250 mg of each compound and pressed with a uniaxial pressure of 374 MPa for 3 min. The measurements were controlled using the software ECLab V 13.0, while a temperature profile from −40 to 60 °C in 10 °C steps was applied in a *Biologic* climate chamber. Impedance spectra were recorded with a perturbation amplitude of 10 mV over a frequency range of 50 mHz to 7 MHz and analyzed with RelaxIS 3. To further investigate grain boundary contributions, the sample processed at 500 rpm for 240 min was pelletized, isostatically pressed at 413 MPa for 30 min, sputtered with a layer of gold and measured in a pouch cell at -100 °C with an Alpha-A impedance analyzer from Novocontrol Technologies applying an AC excitation voltage of 10.6 mV in a frequency range from 10 MHz to 50 mHz.

Preparation of Cathode Composites: $LiNi_{0.83}Co_{0.11}Mn_{0.06}O_2$ (MSE supplies, 140 mg, 70 weight-%) and the respective $Li_{5.5}PS_{4.5}Cl_{1.5}$ sample (60 mg, 30 weight-%) were scaled under inert conditions and mixed in a Fritsch PULVERISETTE 23 mill with 2 g of grinding media (ZrO_2, 3 mm diameter) at 15 Hz for 15 min.

Effective Ionic Conductivities: Determined in symmetrical cells: 100 mg of cathode composites were filled in press cells under inert conditions and pressed with a uniaxial pressure of 374 MPa for 3 min. A separator layer of pristine $Li_{5.5}PS_{4.5}Cl_{1.5}$ (80 mg) was added on each side and pressed again with a uniaxial pressure of 374 MPa for 3 min. A layer of indium foil (chemPUR, 99.99%, 100 µm thickness, 9 mm diameter) and lithium foil (Li, abcr, 99.8%, 1.5 mg) were added on both sides. The cell was equilibrated at 25 °C for 6 h under a pressure of 50 MPa and a PEIS measurement at a perturbation amplitude of 10 mV over a frequency range of 50 mHz to 7 MHz. The spectra were analyzed with RelaxIS 3 using the T-type transmission line model.[47]

Electrochemical Rate Performance Tests: Press cells were filled with cathode composite (12 mg) and pristine $Li_{5.5}PS_{4.5}Cl_{1.5}$ (60 mg) and densified with a uniaxial pressure of 374 MPa for 3 min. Indium foil (9 mm diameter) and lithium foil (1.5 mg) were added on top of the separator. Cells were equilibrated at 25 °C for 6 h under a pressure of 50 MPa and then cycling tests at rates of 0.05 C (0.107 mA cm^{-2}), 0.1 C (0.214 mA cm^{-2}), 0.2 C (0.428 mA cm^{-2}), 0.5 C (1.070 mA cm^{-2}), 1 C (2.140 mA cm^{-2}) and again at 0.05 C were performed with the MACCOR for 5 charge–discharge cycles per cycling rate. Final cycling tests at a rate of 0.05 C had to be remeasured after an erroneous cycling protocol in the last rate step.

Supporting Information

Supporting Information is available from the Wiley Online Library or from the author.

Acknowledgements

The research was supported by the International Graduate School for Battery Chemistry, Characterization, Analysis, Recycling and Application (BACCARA), which is funded by the Ministry for Culture and Science of North Rhine Westphalia, Germany. The authors acknowledge financial support within the cluster of competence FESTBATT funded by the Bundesministerium für Bildung und Forschung (BMBF; projects 03XP0430A, 03XP0430F, 03XP0430C). The authors further acknowledge funding from the Deutsche Forschungsgemeinschaft under project number 459785385. HMRW thanks the FFG (Austrian Research Promotion Agency) for financial support within the project safeLIB. This research used resources at the Spallation Neutron Source, a DOE Office of Science User Facility operated by the Oak Ridge National Laboratory.

Open access funding enabled and organized by Projekt DEAL.

Conflict of Interest

The authors declare no conflict of interest.

Data Availability Statement

The data that support the findings of this study have been archived at https://doi.org/10.17879/06978410383.

Keywords

argyrodite, mechanical milling, processing, solid electrolytes, solid state batteries

Received: July 26, 2024
Revised: August 20, 2024
Published online: September 5, 2024

[1] J. Janek, W. G. Zeier, *Nat. Energy* **2016**, *1*, 16141.
[2] K. B. Hatzell, X. C. Chen, C. L. Cobb, N. P. Dasgupta, M. B. Dixit, L. E. Marbella, M. T. McDowell, P. P. Mukherjee, A. Verma, V. Viswanathan, A. S. Westover, W. G. Zeier, *ACS Energy Lett.* **2020**, *5*, 922.
[3] T. Krauskopf, F. H. Richter, W. G. Zeier, J. Janek, *Chem. Rev.* **2020**, *120*, 7745.
[4] J. A. Lewis, K. A. Cavallaro, Y. Liu, M. T. McDowell, *Joule* **2022**, *6*, 1418.
[5] D. H. S. Tan, Y.-T. Chen, H. Yang, W. Bao, B. Sreenarayanan, J.-M. Doux, W. Li, B. Lu, S.-Y. Ham, B. Sayahpour, J. Scharf, E. A. Wu, G. Deysher, H. E. Han, H. J. Hah, H. Jeong, J. B. Lee, Z. Chen, Y. S. Meng, *Carbon Science* **2021**, *373*, 1494.
[6] J. Janek, W. G. Zeier, *Nat. Energy* **2023**, *8*, 230.
[7] R. Murugan, V. Thangadurai, W. Weppner, *Angew. Chem., Int. Ed.* **2007**, *46*, 7778.
[8] M. M. Raju, F. Altayran, M. Johnson, D. Wang, Q. Zhang, *Electrochem* **2021**, *2*, 390.
[9] J. Awaka, A. Takashima, K. Kataoka, N. Kijima, Y. Idemoto, J. Akimoto, *Chem. Lett.* **2011**, *40*, 60.
[10] X. Li, J. Liang, N. Chen, J. Luo, K. R. Adair, C. Wang, M. N. Banis, T.-K. Sham, L. Zhang, S. Zhao, *Angew. Chem.* **2019**, *131*, 16579.
[11] R. Schlem, A. Banik, S. Ohno, E. Suard, W. G. Zeier, *Chem. Mater.* **2021**, *33*, 327.
[12] P. Bron, S. Johansson, K. Zick, J. Schmedt auf der Günne, S. Dehnen, B. Roling, *J. Am. Chem. Soc.* **2013**, *135*, 15694.
[13] Y. Kato, R. Saito, M. Sakano, A. Mitsui, M. Hirayama, R. Kanno, *J. Power Sources* **2014**, *271*, 60.
[14] L. Zhou, N. Minafra, W. G. Zeier, L. F. Nazar, *Acc. Chem. Res.* **2021**, *54*, 2717.
[15] H.-J. Deiseroth, S.-T. Kong, H. Eckert, J. Vannahme, C. Reiner, T. Zaiß, M. Schlosser, *Angew. Chem., Int. Ed.* **2008**, *47*, 755.
[16] N. J. J. de Klerk, I. Rosłoń, M. Wagemaker, *Chem. Mater.* **2016**, *28*, 7955.
[17] A. Gautam, M. Sadowski, N. Prinz, H. Eickhoff, N. Minafra, M. Ghidiu, S. P. Culver, K. Albe, T. F. Fässler, M. Zobel, W. G. Zeier, *Chem. Mater.* **2019**, *31*, 10178.
[18] A. R. Stamminger, B. Ziebarth, M. Mrovec, T. Hammerschmidt, R. Drautz, *Chem. Mater.* **2019**, *31*, 8673.
[19] K. Hogrefe, N. Minafra, I. Hanghofer, A. Banik, W. G. Zeier, H. M. R. Wilkening, *J. Am. Chem. Soc.* **2022**, *144*, 1795.
[20] A. Gautam, M. Ghidiu, E. Suard, M. A. Kraft, W. G. Zeier, *ACS Appl. Energy Mater.* **2021**, *4*, 7309.
[21] W. Jiang, X. Zhu, R. Huang, S. Zhao, X. Fan, M. Ling, C. Liang, L. Wang, *Adv. Energy Mater.* **2022**, *12*, 2103473.
[22] S. Yanev, C. Heubner, K. Nikolowski, M. Partsch, H. Auer, A. Michaelis, *J. Electrochem. Soc.* **2024**, *171*, 020512.
[23] C. Fu, G. Homann, R. Grissa, D. Rentsch, W. Zhao, T. Gouveia, A. Falgayrat, R. Lin, S. Fantini, C. Battaglia, *Adv. Energy Mater.* **2022**, *12*, 2200412.

© 2024 The Author(s). Advanced Energy Materials published by Wiley-VCH GmbH

16146840, 2025, 5, Downloaded from https://advanced.onlinelibrary.wiley.com/doi/10.1002/aenm.202403291 by Forschungszentrum Jülich GmbH Research Center, Wiley Online Library on [16/07/2025]. See the Terms and Conditions (https://onlinelibrary.wiley.com/terms-and-conditions) on Wiley Online Library for rules of use; OA articles are governed by the applicable Creative Commons License

[24] M. Nagao, A. Hayashi, M. Tatsumisago, *Electrochim. Acta* **2011**, *56*, 6055.
[25] T. Hakari, A. Hayashi, M. Tatsumisago, *Adv. Sustainable Syst.* **2017**, *1*, 1700017.
[26] S. E. Sandoval, J. A. Lewis, B. S. Vishnugopi, D. L. Nelson, M. M. Schneider, F. J. Q. Cortes, C. M. Matthews, J. Watt, M. Tian, P. Shevchenko, P. P. Mukherjee, M. T. McDowell, *Joule* **2023**, *7*, 2054.
[27] L. Schweiger, K. Hogrefe, B. Gadermaier, J. L. Rupp, H. M. R. Wilkening, *J. Am. Chem. Soc.* **2022**, *144*, 9597.
[28] L. Peng, C. Yu, Z. Zhang, R. Xu, M. Sun, L. Zhang, S. Cheng, J. Xie, *Energy & Environmental Mater.* **2023**, *6*, e12308.
[29] Y. Wang, H. Hao, K. G. Naik, B. S. Vishnugopi, C. D. Fincher, Q. Yan, V. Raj, H. Celio, G. Yang, H. Fang, Y.-M. Chiang, F. A. Perras, P. Jena, J. Watt, P. P. Mukherjee, D. Mitlin, *Adv. Energy Mater.* **2024**, *14*, 2304530.
[30] G. F. Dewald, S. Ohno, J. G. Hering, J. Janek, W. G. Zeier, *Batteries Supercaps* **2021**, *4*, 183.
[31] A. Banik, T. Famprikis, M. Ghidiu, S. Ohno, M. A. Kraft, W. G. Zeier, *Chem. Sci.* **2021**, *12*, 6238.
[32] C. Wei, C. Yu, L. Peng, Z. Zhang, R. Xu, Z. Wu, C. Liao, W. Zhang, L. Zhang, S. Cheng, J. Xie, *Mater. Adv.* **2022**, *3*, 1047.
[33] R. C. Howell, T. Proffen, S. D. Conradson, *Phys. Rev. B* **2006**, *73*, 094107.
[34] D. Balzar, N. Audebrand, M. R. Daymond, A. Fitch, A. Hewat, J. I. Langford, A. Le Bail, D. Louër, O. Masson, C. N. McCowan, N. C. Popa, P. W. Stephens, B. H. Toby, *J. Appl. Crystallogr.* **2004**, *37*, 911.
[35] G. K. Williamson, W. H. X-R Hall, *Acta Metall.* **1953**, *1*, 22.
[36] M. A. R. Miranda, J. M. Sasaki, *Acta Crystallographica Section A: Foundations and Advances* **2018**, *74*, 54.
[37] R. Schlenker, A.-L. Hansen, A. Senyshyn, T. Zinkevich, M. Knapp, T. Hupfer, H. Ehrenberg, S. Indris, *Chem. Mater.* **2020**, *32*, 8420.
[38] P. Wang, H. Liu, S. Patel, X. Feng, P.-H. Chien, Y. Wang, Y.-Y. Hu, *Chem. Mater.* **2020**, *32*, 3833.
[39] H. Hertz, *Journal für die reine und angewandte Mathematik* **2009**, *1882*, 156.
[40] R. D. Mindlin, *J. Appl. Mech* **1949**, *16*, 259.
[41] M. Hofer, M. Grube, C. F. Burmeister, P. Michalowski, S. Zellmer, A. Kwade, *Adv. Powder Technol.* **2023**, *34*, 104004.
[42] A. Kwade, *Chem. Eng. Technol.* **2003**, *26*, 199.
[43] N. Bloembergen, E. M. Purcell, R. V. Pound, *Phys. Rev.* **1948**, *73*, 679.
[44] A. Jodlbauer, J. Spychala, K. Hogrefe, B. Gadermaier, H. M. R. Wilkening, *Chem. Mater.* **2024**, *36*, 1648.
[45] M. Gombotz, C. Hiebl, F. Stainer, H. M. R. Wilkening, *J. Phys. Chem. C* **2023**, *127*, 10960.
[46] M. A. Kraft, S. P. Culver, M. Calderon, F. Böcher, T. Krauskopf, A. Senyshyn, C. Dietrich, A. Zevalkink, J. Janek, W. G. Zeier, *J. Am. Chem. Soc.* **2017**, *139*, 10909.
[47] S. Ohno, T. Bernges, J. Buchheim, M. Duchardt, A.-K. Hatz, M. A. Kraft, H. Kwak, A. L. Santhosha, Z. Liu, N. Minafra, *ACS Energy Lett.* **2020**, *5*, 910.
[48] A. Bielefeld, D. A. Weber, J. Janek, *ACS Appl. Mater. Interfaces* **2020**, *12*, 12821.
[49] E. Schlautmann, A. Weiß, O. Maus, L. Ketter, M. Rana, S. Puls, V. Nickel, C. Gabbey, C. Hartnig, A. Bielefeld, W. G. Zeier, *Adv. Energy Mater.* **2023**, *13*, 2302309.
[50] P. Minnmann, L. Quillman, S. Burkhardt, F. H. Richter, J. Janek, *J. Electrochem. Soc.* **2021**, *168*, 040537.
[51] L. de Biasi, B. Schwarz, T. Brezesinski, P. Hartmann, J. Janek, H. C Ehrenberg, *Adv. Mater.* **2019**, *31*, 1900985.
[52] S. Wang, R. Fang, Y. Li, Y. Liu, C. Xin, F. H. Richter, C.-W. Nan, *J. Materiomics* **2021**, *7*, 209.
[53] A. A. Coelho, *J. Appl. Crystallogr.* **2018**, *51*, 210.
[54] P. Thompson, D. E. Cox, J. B. Hastings, *J. Appl. Crystallogr.* **1987**, *20*, 79.
[55] R. W. Cheary, A. A. Coelho, *Powder Diffr.* **1998**, *13*, 100.
[56] S. L. J. Thomae, N. Prinz, T. Hartmann, M. Teck, S. Correll, M. Zobel, *Rev. Sci. Instrum.* **2019**, *90*, 043905.
[57] P. Juhás, T. Davis, C. L. Farrow, S. J. L. Billinge, *J. Appl. Crystallogr.* **2013**, *46*, 560.
[58] C. L. Farrow, P. Juhas, J. W. Liu, D. Bryndin, E. S. Božin, J. Bloch, T. Proffen, S. J. L. Billinge, *J. Phys.: Condens. Matter* **2007**, *19*, 335219.
[59] B. J. Campbell, H. T. Stokes, D. E. Tanner, D. M. Hatch, *J. Appl. Crystallogr.* **2006**, *39*, 607.
[60] V. Epp, Ö. Gün, H.-J. Deiseroth, M. Wilkening, *Phys. Chem. Chem. Phys.* **2013**, *15*, 7123.
[61] C. F. Burmeister, M. Hofer, P. Molaiyan, P. Michalowski, A. Kwade, *Processes* **2022**, *10*, 692.
[62] F. Frankenberg, M. Kissel, C. F. Burmeister, M. Lippke, J. Janek, A. Kwade, *Powder Technol.* **2024**, *435*, 119403.
[63] W. Zhang, D. A. Weber, H. Weigand, T. Arlt, I. Manke, D. Schröder, R. Koerver, T. Leichtweiss, P. Hartmann, W. G. Zeier, J. Janek, *ACS Appl. Mater. Interfaces* **2017**, *9*, 17835.

© 2024 The Author(s). Advanced Energy Materials published by Wiley-VCH GmbH

16146840, 2025, 5, Downloaded from https://advanced.onlinelibrary.wiley.com/doi/10.1002/aenm.202403291 by Forschungszentrum Jülich GmbH Research Center, Wiley Online Library on [16/07/2025]. See the Terms and Conditions (https://onlinelibrary.wiley.com/terms-and-conditions) on Wiley Online Library for rules of use; OA articles are governed by the applicable Creative Commons License